Microstructure Solidification Maps for Al-10wt%Si Alloys

William Hearn[1], Abdoul-Aziz Bogno[1], Jose Spinelli[1,2]
Jonas Valloton[1], Hani Henein[1]

[1] *Department of Chemical and Materials Engineering*
University of Alberta
Edmonton, AB T6G 2G6 Canada

[2] *Department of Materials Engineering,*
Federal University of São Carlos, São Carlos, SP 13565-905 Brazil

Abstract:

Hypo-eutectic Al-Si alloys are widely used in both the automotive and aerospace industries, however, they still have limited usage as structural materials, due to the inherent morphology of the Si phase that forms within the eutectic structure. This non-ideal Si morphology can be modified, via alloy additions and/or rapid solidification (RS), but the underlying mechanism(s) behind this is poorly understood. This work focused on understanding the influence of RS on the eutectic structure, for hypo-eutectic Al-10wt%Si alloys produced by Impulse Atomization and Differential Scanning Calorimetry. This study found that the eutectic Si forms into four distinct morphologies: (1) flaky, (2) fibrous, (3) globular + fibrous and (4) globular, depending on the solidification conditions. As a result, two solidification maps of the Si morphology are proposed, one based on local eutectic solidification conditions and another based on a solidification continuous cooling diagram (SCCT). Both maps help identify the required conditions for certain Si morphologies to form. Hardness measurements were also carried out and it was found that the Si morphology would influence the alloy hardness, with the highest value being achieved when the eutectic Si was globular. This result indicates that the Si morphology is an important factor that can alter the mechanical properties of hypo-eutectic Al-Si alloys.

1 INTRODUCTION

The hypo-eutectic Al-Si alloy system is known for its strong corrosion resistance, good castability and relatively high strength-to-weight ratio [1]. These characteristics make it an important alloy system and has led to its widespread usage in both the automotive and aerospace industries [2]. However, even with these desirable properties, hypo-eutectic Al-Si alloys have limited usage as structural materials, due to the inherent characteristics of the Si phase that forms within its eutectic structure.

In the as-cast state, eutectic Si forms a flaky lamellar morphology that, combined with the inherent brittle nature of Si, significantly reduces the ductility and mechanical property performance. It is possible to modify the Si into a fibrous and rod-like shape, which can yield a 50% improvement in the tensile strength, and a three-fold improvement in the ductility [3].

To achieve this refinement, the typical methods are the use of alloy additions or the control of the solidification conditions [3]. Alloying additions modify the Si by restricting its nucleation or by restricting its growth [4] [5] [6] [7]. While the solidification conditions achieve refinement by controlling the cooling rate, where an increase in the cooling rate will make the Si more fibrous and rod-like [8] [9]. Even though Si can be modified using either technique how this modification occurs is poorly understood, especially the refinement caused by high cooling rates.

It is reported in the work of Khan and Elliott [10] that the transition in Si growth from bulky/faceted plates to smooth/globular fibers is accompanied by a drop in undercooling. This suggests that fibrous growth is a departure from the normal growth of broad faceted flakes toward continuous growth of a non-faceted phase. However, currently no mechanism can explain how Si morphology may be refined, which makes it difficult to reliably predict or design solidification processes to produce Al-Si alloys with the desired Si morphology.

Solidification studies related to the high cooling rate production of Al-Si alloys have been conducted previously. Trivedi [11] and Kalay [12] developed a map of the Al-Si system that described the influence of alloy composition and undercooling. Pierantoni et al. [13] defined the Al-rich boundary of the coupled eutectic zone, at Si compositions between 15.5 to 26 wt.% Si. Although both were beneficial to our understanding, the works only examined the components that

would form, rather than the morphology of the eutectic structure. Moreover, they dealt with eutectic/hypereutectic alloy compositions, and not hypo-eutectic.

This paper investigates the microstructural evolution of rapidly solidified hypo-eutectic Al-10wt%Si alloys, using Impulse Atomization (IA) and Differential Scanning Calorimetry (DSC) techniques. The focus was to develop microstructure maps of the eutectic structure to define what solidification rates would cause shifts in the Si morphology. With these shifts also being related to the mechanical properties of the alloy via Vickers hardness measurements.

2 EXPERIMENTAL PROCEDURE

2.1 MATERIALS & METHODS

In this work 350 g of Al-10wt%Si alloys were produced by induction melting commercial purity Al (99.9%) and high purity Si (99.999%). Various thermal histories were obtained by IA (high cooling rate and large undercooling) and by DSC (low cooling rate and small undercooling). Powders of sizes varying from 125 μm to 1080 μm were generated by IA under helium, then under argon, from a superheated melt (~200 above the melting temperature of the alloy), so that samples with a wide range of cooling rates and undercoolings were obtained. A detailed description of the IA is given elsewhere [14]. A summary of the investigated samples generated by IA is given in Table 1.

Table 1: Summary of the investigated Al-10wt% Si samples generated by IA.

Atomization atmosphere	Atomization temperature (℃)	Powder size range (μm)
Argon	765	125-150
		150-180
		212-250
		300-355
		355-425
		425-500
		212-250
		300-355

Helium	765	425-500 600-710 850-1000 1000-1180

To obtain samples from much lower cooling rates and smaller undercoolings, a small piece of the alloy was solidified in a Setaram Labsys Evo 1600 differential scanning calorimeter (DSC) using two alumina crucibles (sample and reference) and a Pt-Rh DSC rod [15]. Temperature regulation was done on the sample by means of an S-type thermocouple (Pt/Pt-10% Rh), and the sample was heated in a protective flowing argon atmosphere. Scanning rates of 0.01°C/s, 0.02°C/s, 0.08°C/s, 0.2°C/s, 0.3°C/s and 0.8°C/s were applied during both heating and cooling of the sample to and from 800°C to 200°C so that controlled solidification microstructure were obtained.

2.2 ANALYSIS TOOLS & TECHNIQUES

For metallographic analysis, the samples were ground, polished and etched using either Keller's reagent or HCl. Micrographs were collected using a Zeiss Sigma 300 VP-Field Emission Scanning Electron Microscope (FE-SEM). EBSD analysis with the Zeiss Sigma FE-SEM was also done to determine the growth mode of the eutectic Si phase.

X-ray diffraction (XRD) analysis was carried out to identify the precipitated phases during solidification. This analysis was achieved using a Rigaku Powder X-ray diffractometer, over an angular range of 5° to 90°, at a step-size of 0.02° and a dwell time of 0.6s per step. The current and voltage of the X-ray tube was 38 mA and 38 kV respectively, while the radiation was Co-Kα with a wavelength of 1.78899$\dot{A}$.

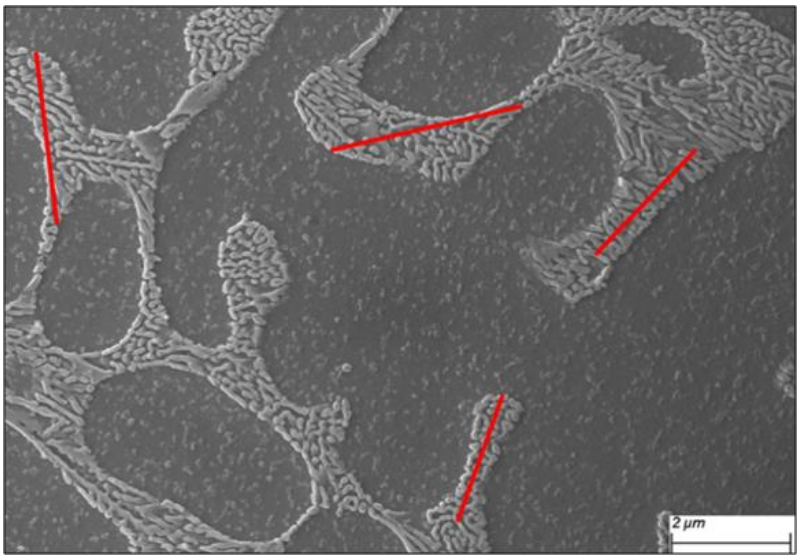

Figure 1: Characteristic linear intercept measurements used to determine the eutectic Si spacing. Shown is an IA Al-10Si particle produced using helium, at a particle size of 212-250µm.

Measurements of the eutectic fraction were carried out via optical micrographs of individual IA particles (using the software ImageJ). Initially, the optical micrograph of a single particle was converted to a binary format. In this binary form, ImageJ could measure the eutectic area fraction and in turn, determine the eutectic weight fraction of a powder. These eutectic fraction measurements were conducted for powders in each examined size range and involved 12 to 15 measurements per size range.

The measurement of the eutectic Si spacing was performed using the linear intercept method [16], with characteristic measurements being shown in Figure 1. For the Si spacing measurements of the IA Al-10wt%Si alloy, 4 to 6 different powders were examined for each investigated size range. The spacing measurements were done at different regions (4 to 7) per powder, using at least 10 measurements per examined region. For the Si spacing measurements of the DSC Al-10wt%Si alloy, at least 10 measurements were done per examined region.

The measured eutectic Si spacing was used to determine the location of eutectic nucleation within an IA powder. With the nucleation region being the area within the microstructure, that had the smallest Si spacing. As it had been shown in previous work that the smallest spacing referred to the largest local eutectic growth rate [17] [18].

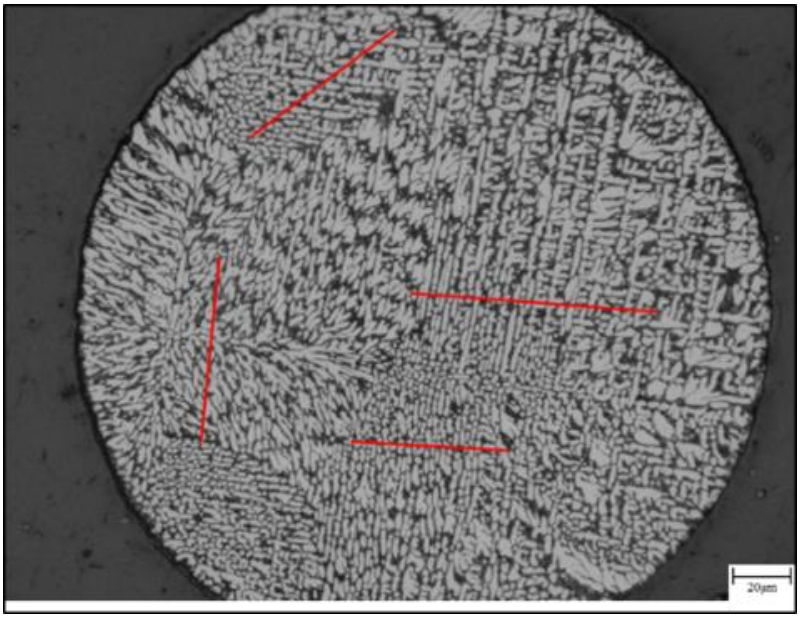

Figure 2: Characteristic linear intercept measurements used to determine the pro-eutectic α-Al spacing. Shown is an IA Al-10Si particle produced using helium, at a particle size of 212-250µm.

The measurement of the pro-eutectic α-Al dendrite cell spacing was conducted using the linear intercept method [16], with characteristic measurements being shown in Figure 2. For each size range, 10 to 14 powders had their α-Al cell spacing measured, with 5 to 7 measurements being conducted for each examined powder.

To characterize the mechanical properties of the Al-10wt%Si alloy, Vickers hardness measurements were conducted using a Buhler VH 3100 hardness machine, at a load of 0.2N and a dwell time of 10s. For each size range, 30-40 indentations / hardness measurements were done.

3 Results & Discussion

3.1 Microstructure & The Influence of Processing History

Characteristic microstructures of the Al-10wt%Si samples solidified by DSC are shown in Figure 3. As can be seen, the microstructure of these samples consists of islands of pro-eutectic α-Al phases (dark) surrounded by α-Al + Si eutectic structures (brighter needles are eutectic Si). It is worth noting that the Fe-impurities appearing within the microstructure in the form of Fe-rich (brightest phases), are the result of 0.07% Fe content in the original alloy, as determined by chemical analysis carried out according to ASTM E1097-12 and ASTM E1479-16.

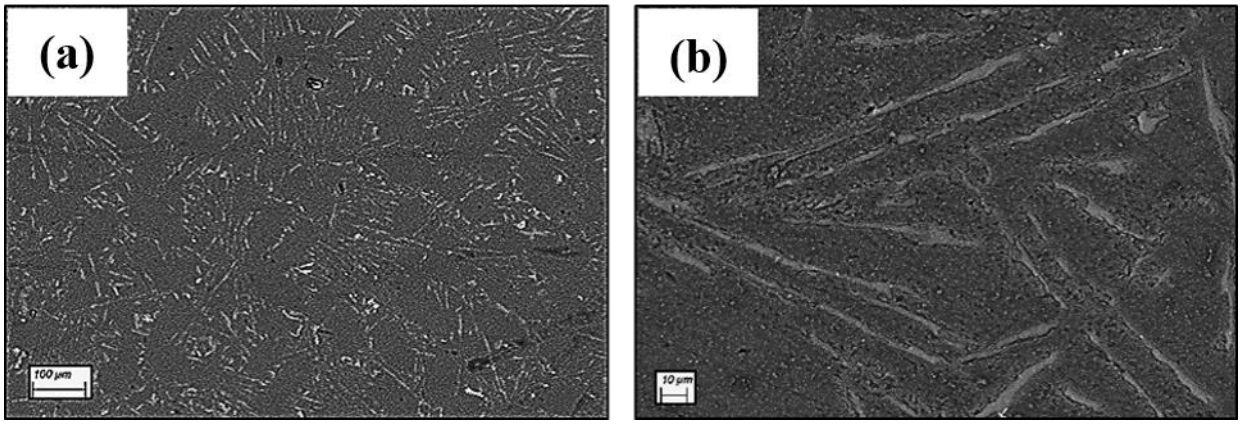

Figure 3: Typical microstructure of an Al-10Si alloy produced by DSC. Cooling rate: 5 K/min (~0.1 K/s). (a) Islands of primary α-Al (dark) surrounded by eutectic cells (α-Al +Si), (b) Zoom of a eutectic cell. The lightest phases are Fe-rich compounds.

Characteristic microstructures of the rapidly solidified Al-10wt%Si alloy, atomized in both helium and argon, are shown in Figure 4 and Figure 5 respectively. Although the processing conditions of the two samples are different the inherent phases and overall structure were similar.

Both samples displayed a microstructure with a pro-eutectic α-Al phase and an α-Al + Si eutectic structure. With the darker regions being the pro-eutectic α-Al phase and the lighter regions being the eutectic Si phase. The dark regions located between the Si phase (shown in the magnified images of Figure 4 and Figure 5) are the eutectic α-Al, which has the same structure and near identical composition as the pro-eutectic α-Al.

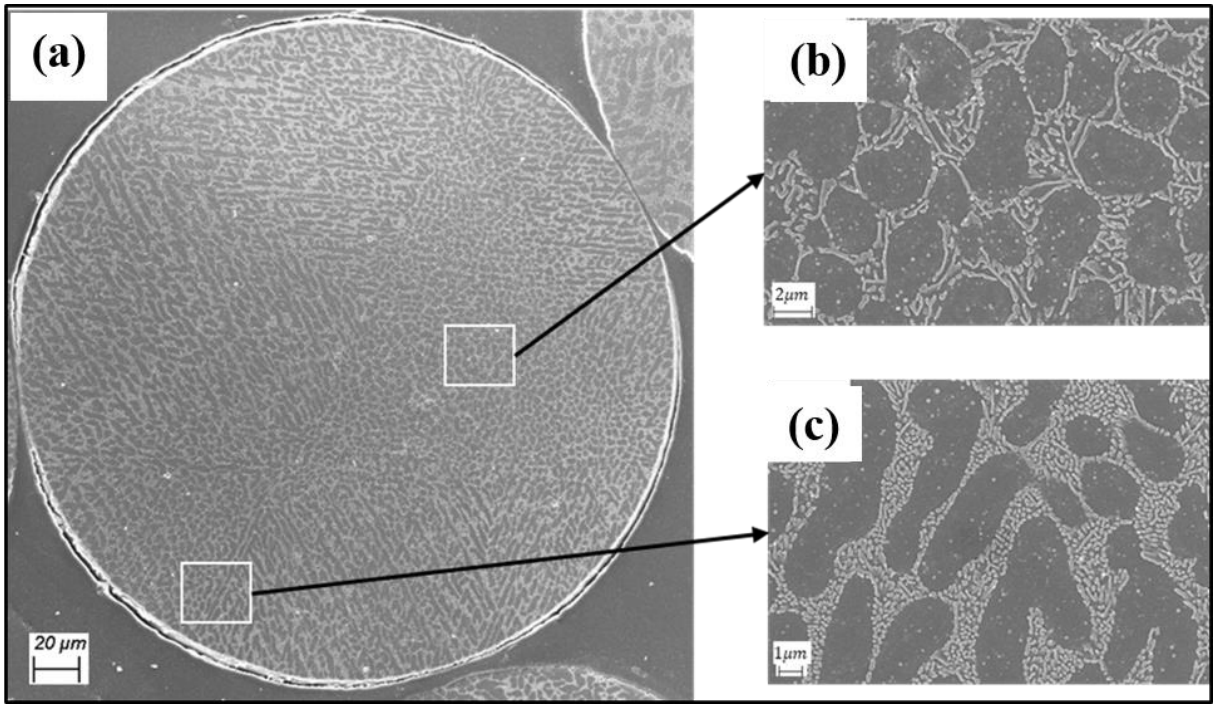

Figure 4: (a) Typical microstructure of Al-10Si droplets atomized in helium (droplet size in the range 300-355 µm); (b) & (c) are higher magnification images highlighting the α-Al + Si eutectic structure.

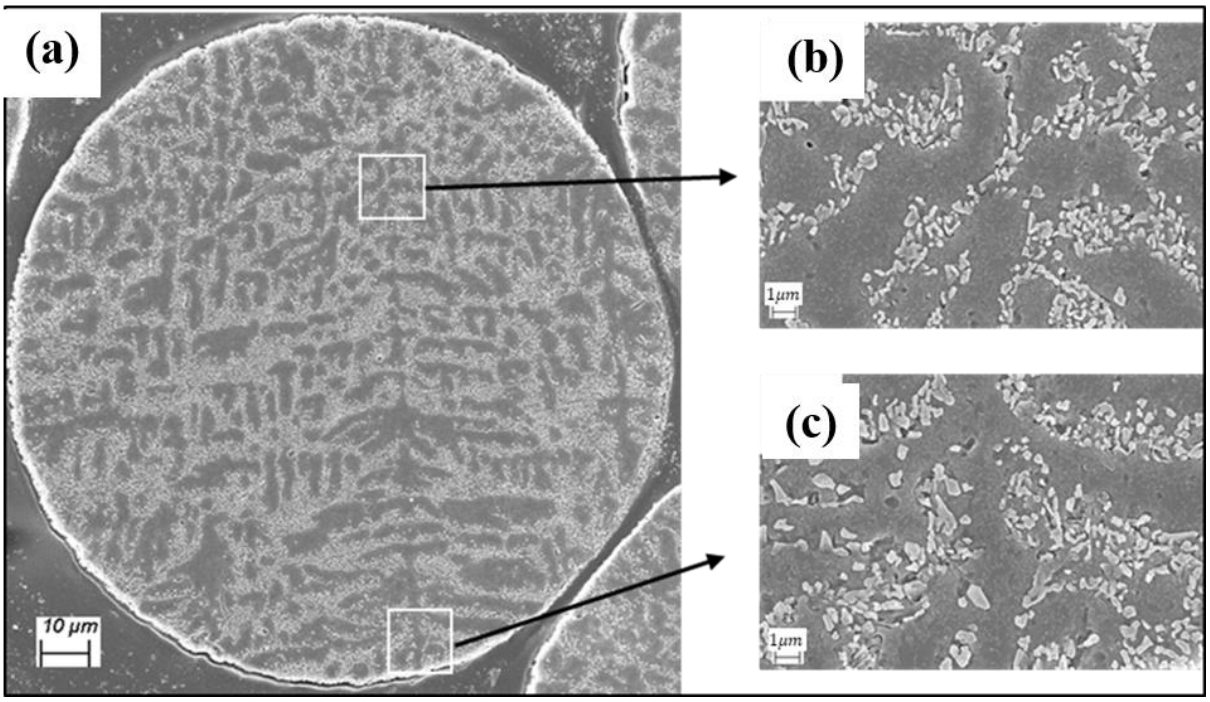

Figure 5: Typical microstructure of an IA Al-10Si alloy produced using argon, at a particle size of 125-150 µm. Images (a) & (b) show higher magnification images to highlight the Al + Si eutectic structure

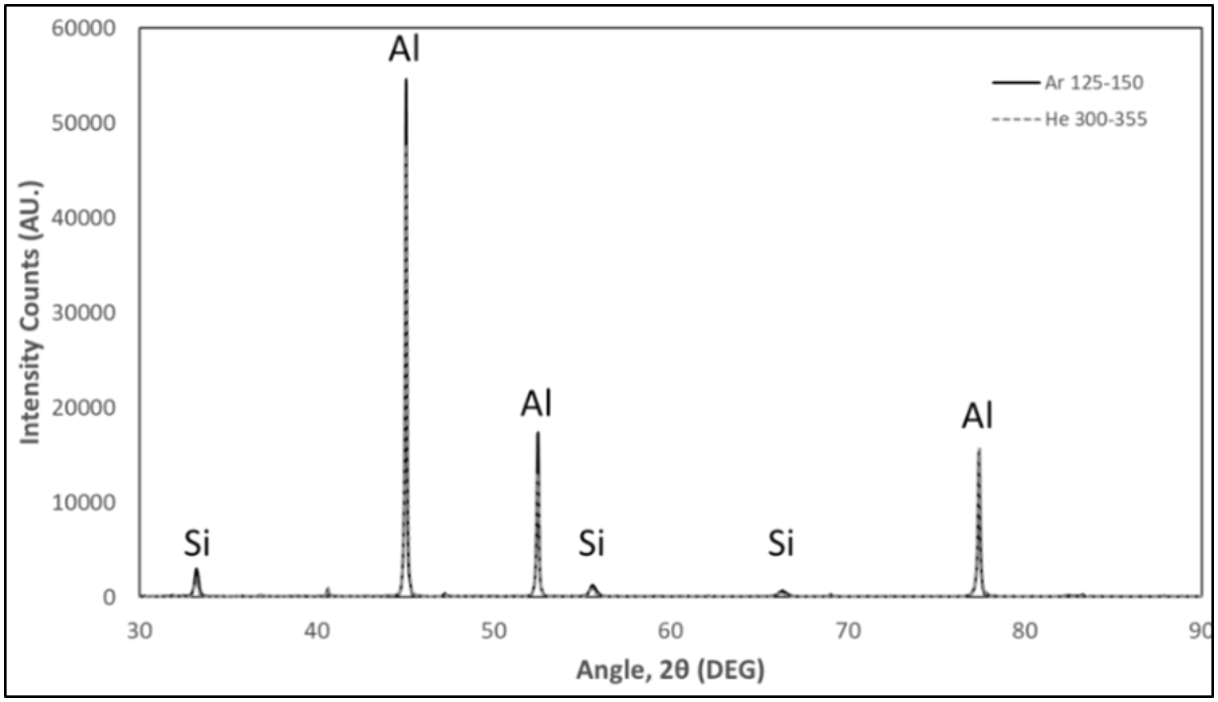

Figure 6: XRD patterns for the Al-10Si alloy produced by IA.

To confirm this finding XRD analysis was carried out on the investigated IA samples. From these results in Figure 6, pattern indexing established a solid solution α-Al phase and a Si phase. Confirming that the major microstructural components were the pro-eutectic α-Al and the α-Al + Si eutectic structure.

Although the inherent components of the two IA samples were similar, the size, spacing and proportion of each varied. Highlighting the dependence of the microstructure on the processing conditions. To examine this in more detail the eutectic fraction, and how it varies with the IA processing conditions, was plotted in Figure 7. The expected eutectic fraction under both equilibrium and Gulliver-Scheil conditions was also included.

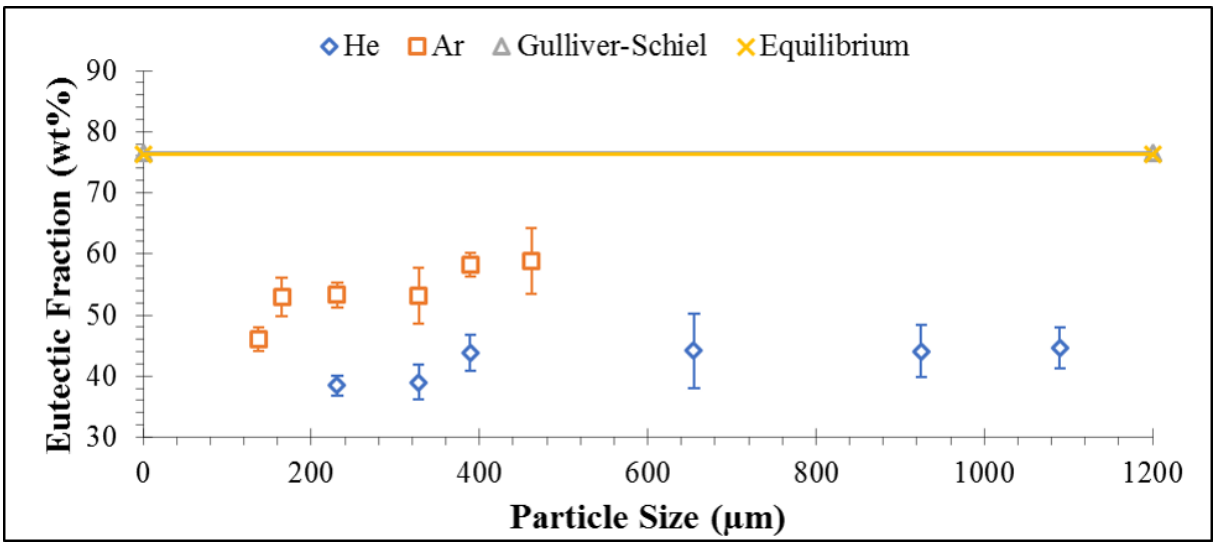

Figure 7: Eutectic fraction of the IA Al-10Si alloy, as a function of the particle size and the atomization gas.

The results in Figure 7 demonstrated two things. First, they show that the amount of eutectic that forms will be dependent on the processing conditions, and thus, the solidification conditions. Where a decrease in the particle size, or the use of helium instead of argon gas, decreases the eutectic fraction. Second, the fraction of these components is lower than what was expected under equilibrium or Gulliver-Scheil conditions. Both results highlight that the solidification of the IA Al-10wt%Si alloy followed a non-equilibrium path.

This deviation from equilibrium shows the rapid solidification nature of IA alloys. However, just using the processing conditions to represent this rapid solidification would make it difficult to compare these results to other works. Therefore, the processing conditions of the IA Al-10wt%Si alloy were related to the liquid cooling rate in Figure 8.

The liquid cooling rate was chosen as it is an important condition that affects each stage of solidification. As well, it is relatively controllable and easy to measure, making this analysis with the liquid cooling rate more applicable to others who would work with Al-10wt%Si alloys under rapid solidification conditions. To estimate the liquid cooling rate a thermal model that describes droplet solidification during IA was used [14] [19]. This model calculates the temperature variation of a superheated IA droplet during solidification, in a stagnant and inert atmosphere. The estimated liquid cooling rates vary from 1×10^3 K/s to 2×10^4 K/s as the size droplet size decreases, for samples atomized in both argon and helium. As expected, for droplets of the same size, helium yields a higher cooling rate thanks to a substantially larger heat capacity and thermal conductivity of the

gas compared to argon. Similar trends, between the droplet size and the solidification rate, have been found in past work [11] [12] [21] [22]. The thermo-physical properties of the two gases are shown in in Table 2.

Table 2: Thermo-physical properties of argon and helium gas [14] [23].

Property	**Units**	**Argon**	**Helium**
Heat Capacity	$Jkg^{-1}K^{-1}$	520	5195
Density	kgm^{-3}	$539.23 \cdot T^{-1.0205}$	$48.14 \cdot T^{-1}$
Conductivity	$10^4 WK^{-1}m^{-1}$	$1.86 \cdot T^{0.7915}$	$38.05 \cdot T^{0.7098}$
Dynamic Viscosity	$10^5 Pa\ s$	$0.0238 \cdot T^{0.7913}$	$0.0367 \cdot T^{0.7}$

Another solidification condition to consider is the coarsening rate of pro-eutectic α-Al phase, defined by the rate of solidification from the end of recalescence to the nucleation of the eutectic structure. This coarsening rate controls the spacing of the pro-eutectic α-Al phase, and in turn, the distribution and fraction of eutectic within the alloy [24] [25] [26]. Making it an important factor that will determine the solidification interval of a given sample and subsequently the primary and secondary nucleation temperatures [27].

To estimate the α-Al coarsening rate, the solidification interval of coarsening must be determined. This interval is the time region between the liquidus temperature and the eutectic nucleation temperature. Meaning that if these temperatures were known, the coarsening solidification rate $\dot{T}$ of the pro-eutectic α-Al phase could be calculated using Equation 1:

$$\dot{T} = \frac{T_L - T'_E}{t_L - t'_E} \quad (1)$$

where T_L is the temperature at the end of recalescence (approximated to the liquidus temperature) and was estimated using the thermal model of a solifiying droplet, described in [14] [19], T'_E is the eutectic nucleation temperature, t_L is the time at which the liquidus temperature occurs and t'_E is the time at which the eutectic nucleation temperature is reached.

To estimate the eutectic nucleation temperature of each sample, the experimentally measured eutectic weight percent was compared to the calculated eutectic fractions (using Gulliver-Scheil equation) along the extended solidus and liquidus lines of the phase diagram. The eutectic nucleation undercooling was found when there is a match between the experimental and calculated eutectic fractions. A more detailed description of this procedure is given elsewhere [27]. The

eutectic nucleation undercooling was subsequently used together with the solidification interval and the α-Al spacing λ, to determine the primary nucleation undercooling. The secondary dendrite arm spacing is related to the cooling rate according to equation 2 [28] [29]:

$$\lambda = B(\dot{T})^{-n} \quad (2)$$

where B and n are alloy-dependent constants obtained in this work from the best fitting curves α-λ Vs $\dot{T}$. For the investigated alloy, Figure 8 shows B and n values of ~55 and ~0.41 respectively, which are in a fairly good agreement with the reported values (dubbed ideal) of 50 and 1/3 for Al alloys [29].

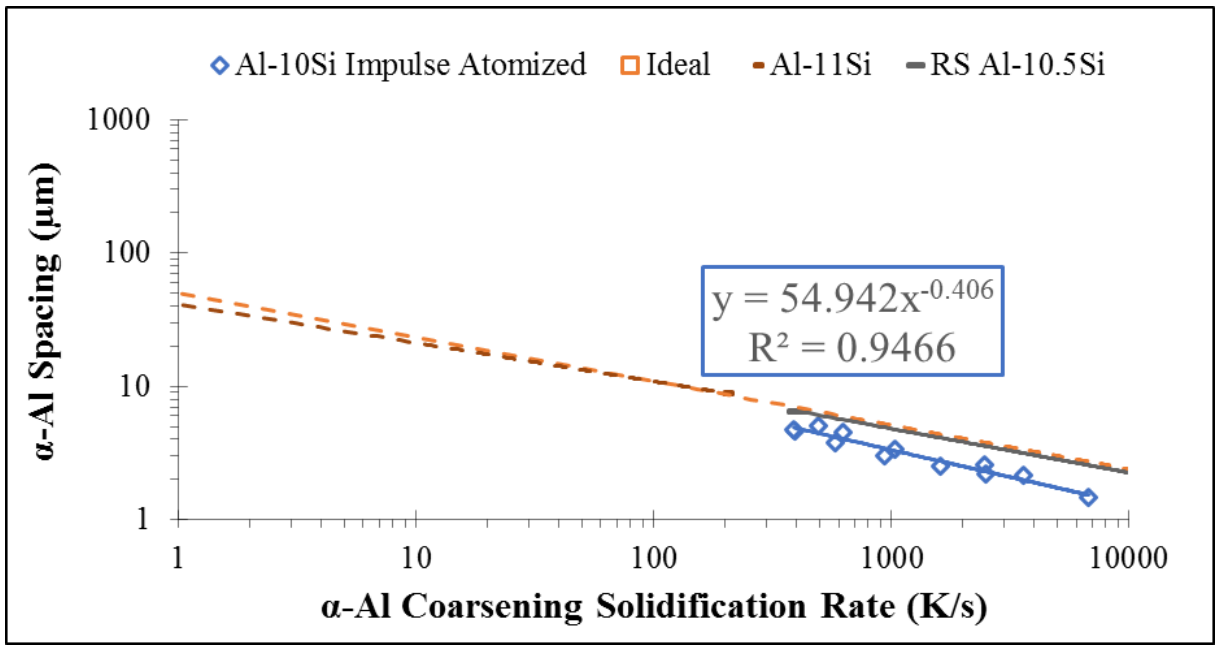

Figure 8: Pro-eutectic α-Al dendrite cell spacing as a function of the coarsening solidification rate. The B & n values for the IA Al-10Si alloy are shown in blue, while the ideal values for Al alloys are shown in orange. This plot also includes the B & n values for Al-Si alloys from the past work of Anyalebechi [30] and Armstrong [31].

Results from past work on Al-Si alloys by Anyalebechi [30] and Armstrong [31] are also included in Figure 8.

3.2 Variation in Eutectic structural scale and Si Morphology

Eutectic silicon spacing was measured and its variation with the liquid cooling rate was analyzed for all the investigated samples.

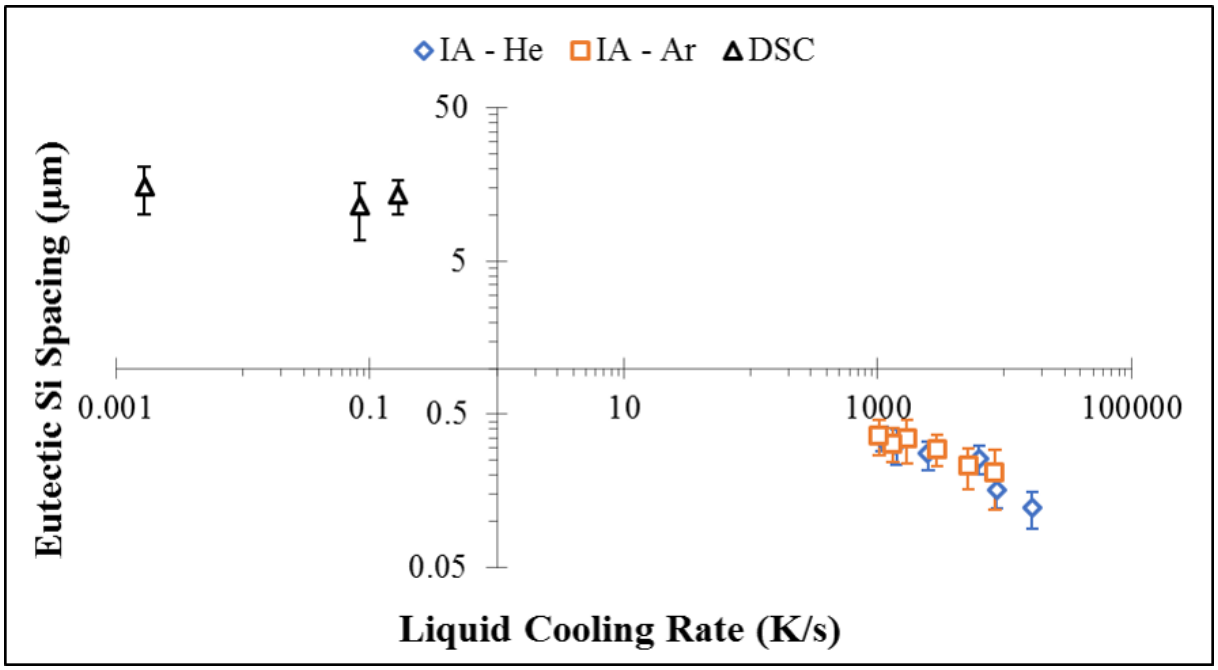

Figure 9: Eutectic Si spacing as a function of the liquid cooling rate for the Al-10wt%Si alloy.

Figure 9 shows that the eutectic Si spacing decreases as the liquid cooling rate increases, confirming a refinement by rapid cooling. However, in order to get a complete understanding of the evolution of the eutectic Si over the range of investigated cooling rates, its morphology is an important factor to consider.

Examining the solidification microstructures of the DSC samples in Figure 3, it can be seen that the eutectic Si has the plate-like morphology that is commonly observed in a cast microstructure. Conversely, in the eutectic structure of the IA samples, shown in Figures 4 and 5, the Si morphology varies, not only between the two particles, but within the same particle as well.

To better define this morphological shift, a qualitative characterization of the eutectic Si morphology was conducted using FE-SEM images. From this analysis, it was found that the Si morphology could be classified into four groups, shown in Figure 10.

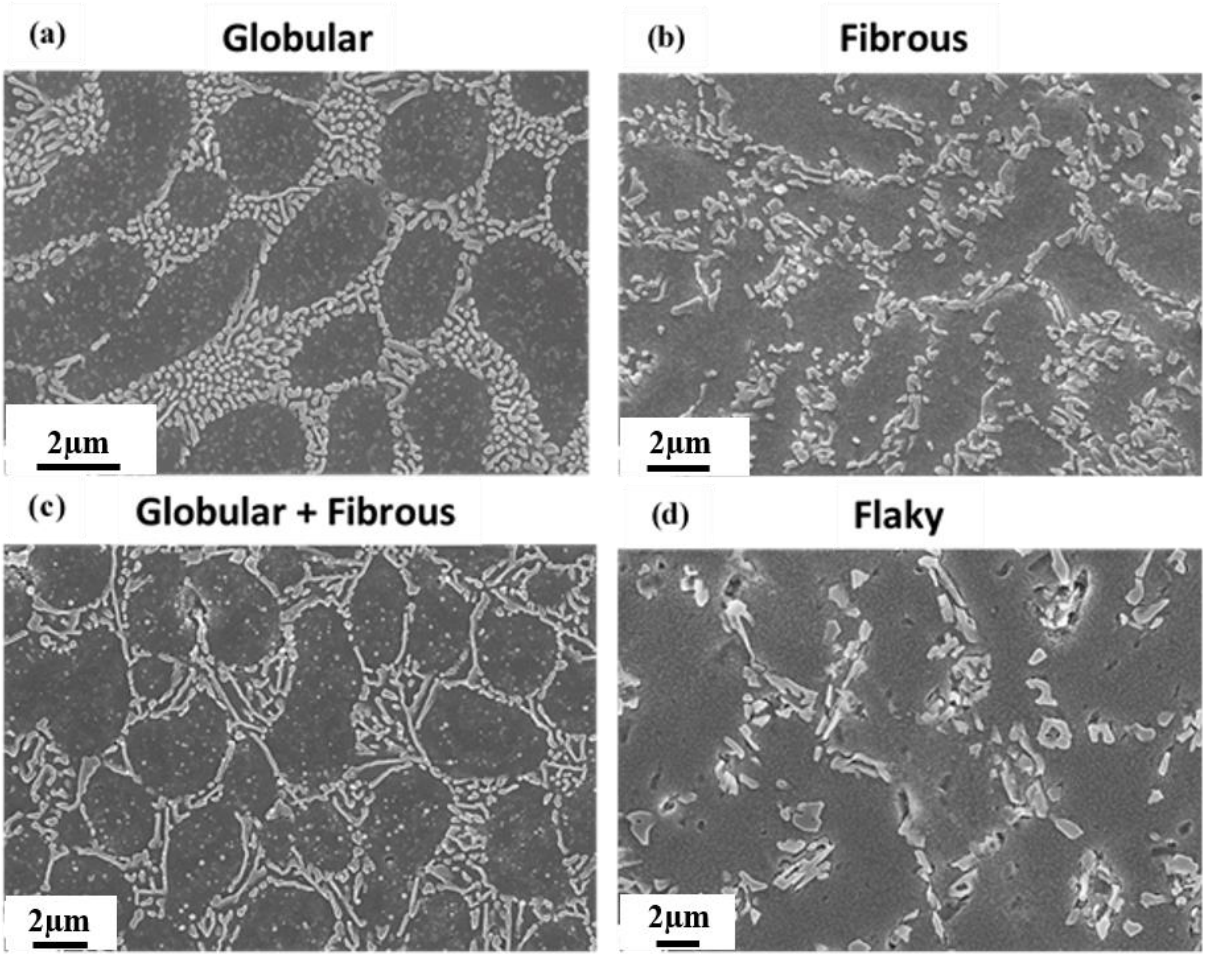

Figure 10: FE-SEM images outlining the four observed morphologies of the eutectic Si phase. (a) "Globular" Si morphology, He 212-250µm sample. (b) Fibrous" Si morphology, Ar 125-150µm sample. (c) "Globular + Fibrous" Si morphology, He 300-355µm sample. (d) "Flaky" Si morphology, Ar 300-355µm sample.

The first grouping relates to a “Globular” Si morphology that is rounded, refined and compact. The second grouping relates to a “Fibrous” Si morphology that has a combination of rounded + sharp features, with an elongated shape. The third grouping relates to a “Globular + Fibrous” Si morphology, that is a combination of rounded + non-elongated Si and sharp + elongated Si. The fourth grouping relates to a “Flaky” Si morphology that is blocky, elongated and not rounded.

From visual analysis, the globular Si was ascribed as the most refined morphology. With the fibrous Si and the flaky Si being considered progressively less refined, as they started to more closely resemble the typical, plate-like Si found in castings. To relate this analysis to quantitative results, the average eutectic Si spacing in each morphological group was plotted in Figure 11.

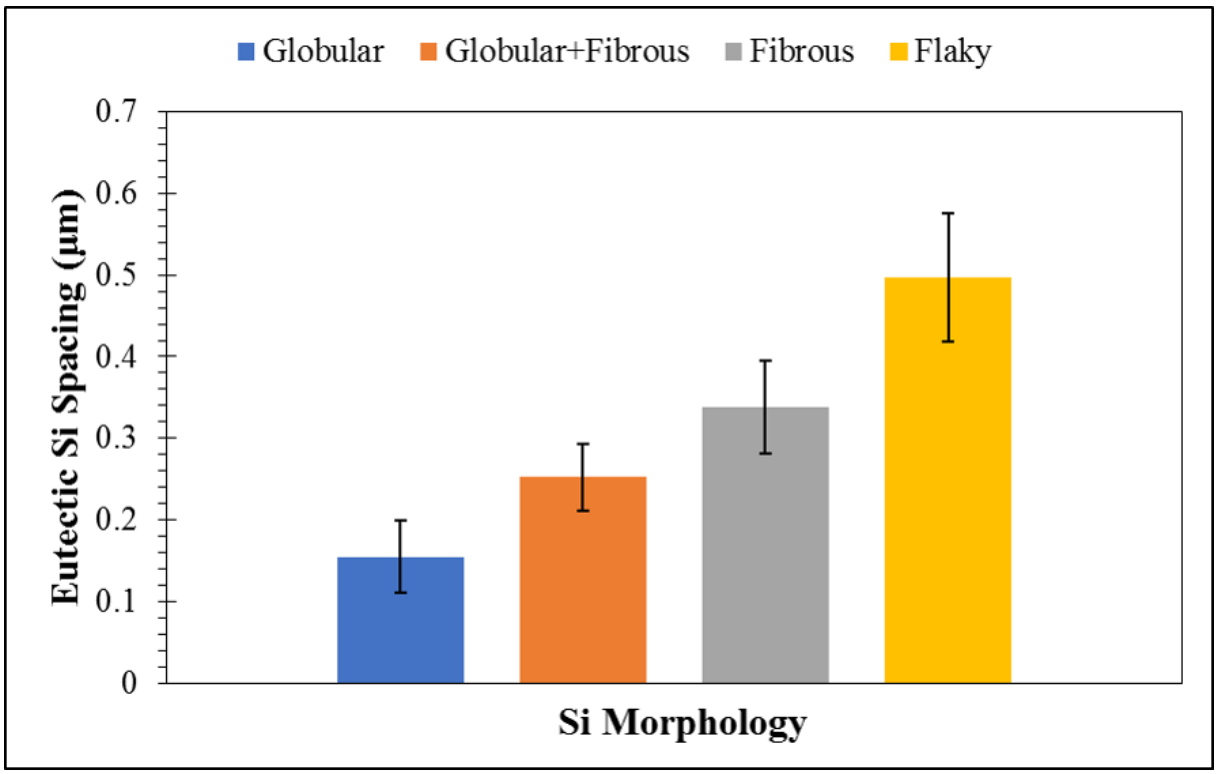

Figure 11: Average eutectic Si interphase spacing of each Si morphology grouping.

Figure 11 clearly shows that as the Si spacing decreases, the morphology will shift from flaky → fibrous → globular + fibrous → globular. This seems to indicate that the observed changes in Si morphology relate to changes in the local growth conditions of the eutectic structure.

The outlined characterization was also used to determine the dominant Si morphology at the eutectic nucleation point (for the IA Al-10wt%Si alloy). The criterion for this determination was not based on what morphology had the most counts and was instead based on the distribution. If the counts were split between various morphologies, then the dominant Si morphology was considered a mix between the two. But if every count was of one morphology then that would be considered the dominant Si morphology. The results of this analysis are shown in Figure 12 as a function of the liquid cooling rate, for samples atomized in both helium and in argon.

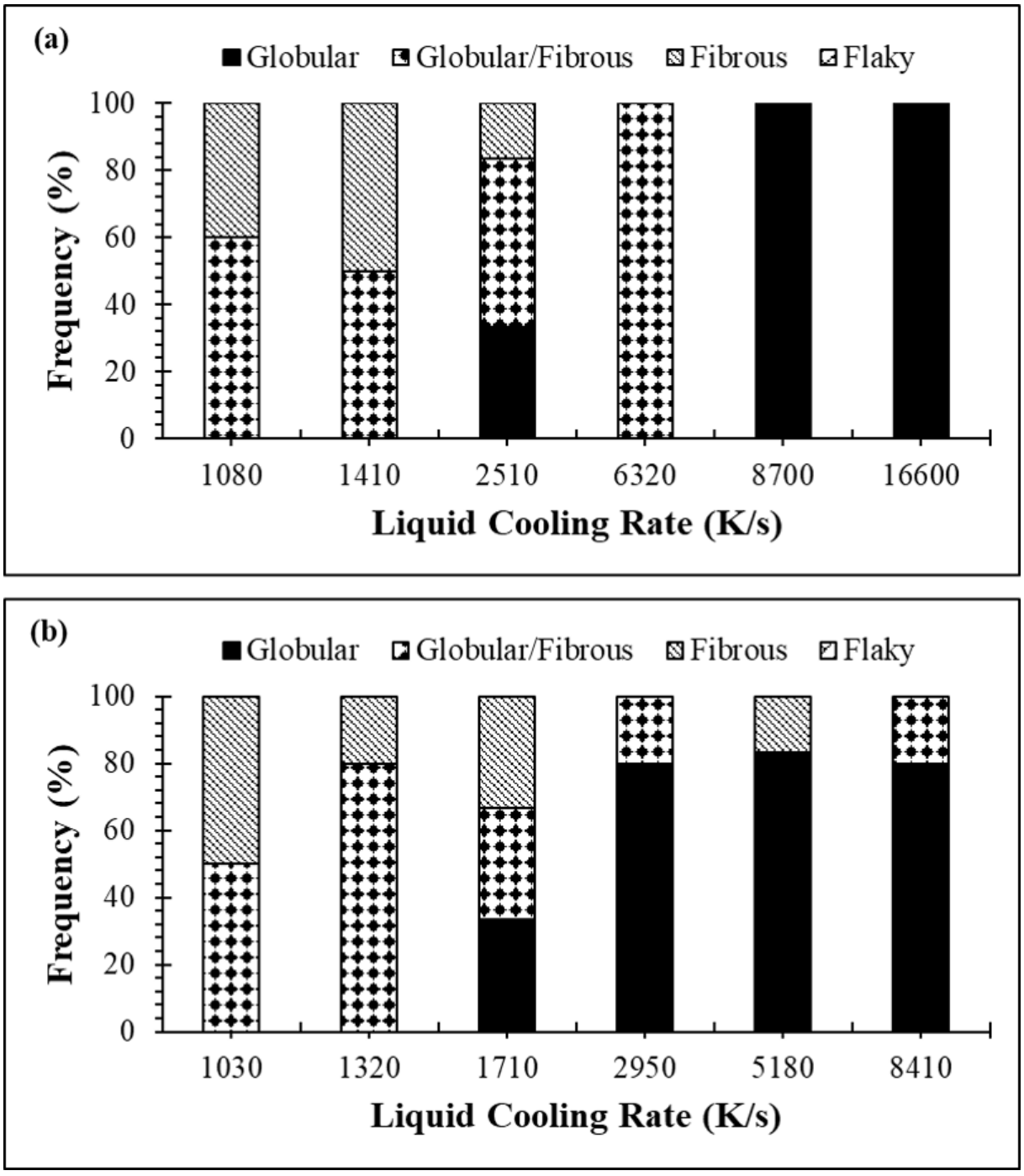

Figure 12: Distribution of the observed Si morphology, around the nucleation point, at specific liquid cooling rates for the IA Al-10Si alloy. As atomized in (a) helium, (b) argon.

The results of this analysis found that a dominant globular morphology prevailed only for samples that were atomized in helium, at the two fastest liquid cooling rates. The rest of the samples showed a mixed globular + fibrous Si morphology.

In more general terms Figure 12 showed that decreases in the liquid cooling rate would shift the Si morphology from globular to globular + fibrous. This result was expected as morphological refinement is expected at higher cooling rates. As well, it was found that if helium was used instead of argon, improved refinement of the Si morphology would occur.

EBSD analysis performed on deeply etched samples (Figure 13), confirmed that in all cases, Si was crystalline, and that the shift in Si morphology was not related to a change in Si growth from crystalline to amorphous.

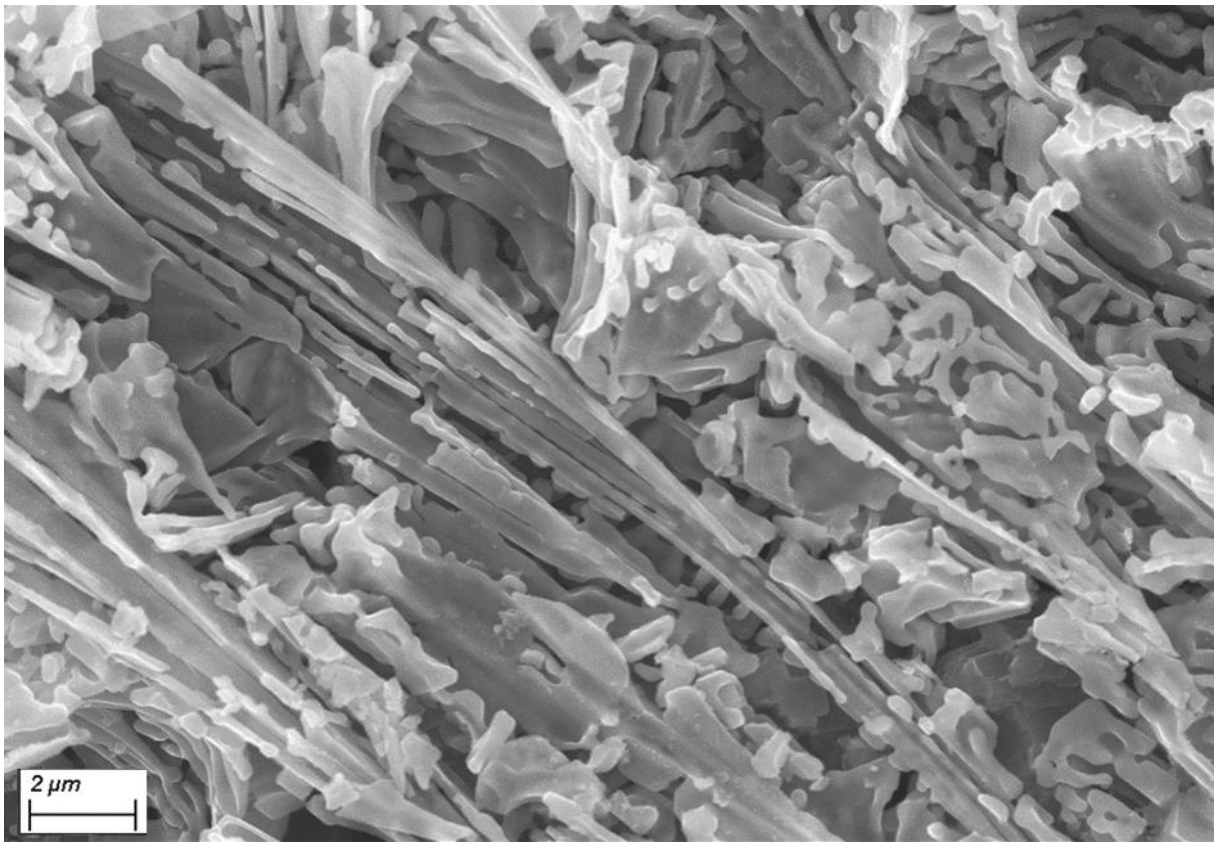

Figure 13: Crystalline Si phase in a deeply etched IA Al-10Si droplet in the size range 300µm - 355µm under Ar.

3.3 LOCAL EUTECTIC SOLIDIFICATION MAP

The qualitative characterization from Section 3.2 suggested that the local eutectic solidification conditions influenced the Si growth morphology. To evaluate this further, methods were developed to estimate the local eutectic solidification conditions so that they could be compared to the Si morphology.

The first set of local solidification conditions to be examined were the growth velocity and the undercooling. Using a modified Jackson-Hunt model [17] this local eutectic undercooling and growth velocity could be described, using the equations (3) to (5).

$$\Delta T_{eut} = (1 + \varphi^2)\frac{K_2}{\lambda} \tag{3}$$

$$v^* = \frac{K_2 \varphi^2}{K_1 \lambda^2} \tag{4}$$

$$K_1 = \left(\frac{mC_o}{D}\right)\left(\frac{P}{f_\alpha f_\beta}\right) \quad \& \quad K_2 = 2m\left(\frac{\Gamma_\alpha \sin\theta_\alpha}{f_\alpha m_\alpha} + \frac{\Gamma_\beta \sin\theta_\beta}{f_\beta m_\beta}\right) \tag{5}$$

where P is a function of the volume fractions ($P = 0.335\left(f_\alpha f_\beta\right)^{1.65}$), K_1 & K_2 are material parameter constants and φ is a dimensionless parameter that is the ratio between the average and the extremum eutectic spacings.

The values of each material property used to calculate K_1 and K_2 can be found in Table 3, while the value of φ was found to be 2.3 for Al-Si alloys [32].

Table 3: Data used for the modified Jackson-Hunt calculations [12] [17] [32] [33].

Parameter Symbol	Parameter Value	Unit	Parameter Name
$\boldsymbol{D}$	4.3E-09	$m^2 s^{-1}$	Diffusion Coefficient
$\boldsymbol{C_o}$	87.7	$wt\%$	Length of weighted eutectic tie-line
$\boldsymbol{m_\alpha}$	7.5	$K.wt\%$	α-phase liquidus slope
$\boldsymbol{m_\beta}$	17.5	$K.wt\%$	β-phase liquidus slope
$\boldsymbol{\Gamma_\alpha}$	1.96E-07	$K.m$	Gibbs-Thompson coefficient α
$\boldsymbol{\Gamma_\beta}$	1.70E-07	$K.m$	Gibbs-Thompson coefficient β
$\boldsymbol{\theta_\alpha}$	30	°	Angle of α-phase
$\boldsymbol{\theta_\beta}$	65	°	Angle of β-phase
$\boldsymbol{T_{eut}}$	850.2	K	Eutectic temperature
$\boldsymbol{C_{eut}}$	0.126	-	Eutectic composition
$\boldsymbol{\Phi}$	2.3	-	Extremum condition parameter
$\boldsymbol{f_\alpha}$	0.873	-	α-phase fraction
$\boldsymbol{f_\beta}$	0.127	-	β-phase fraction

To validate this modified Jackson-Hunt approach the results for the Al-10wt%Si alloy were compared with past results for other Al-Si alloys. This comparison involved a plotting of the eutectic Si spacing as a function of the local eutectic growth velocity, shown in Figure 14.

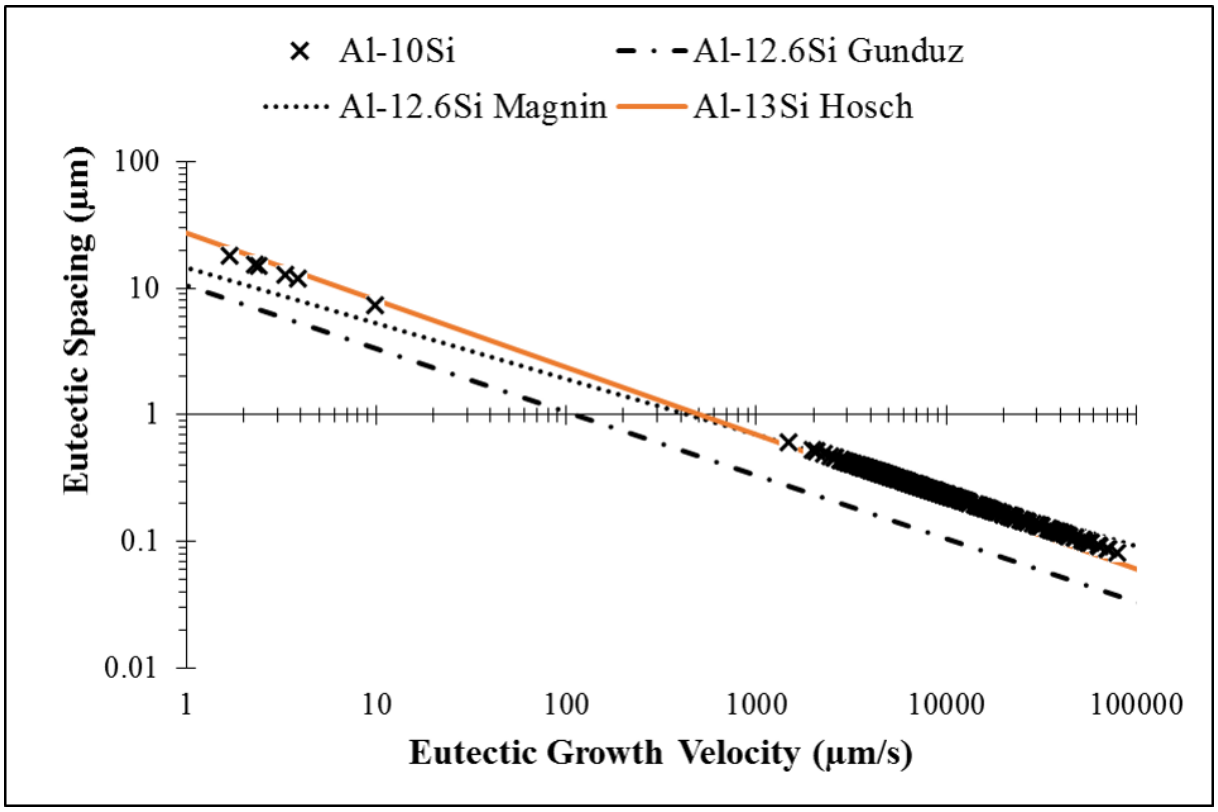

Figure 14: Eutectic Si spacing versus eutectic growth velocity plot for the Al-10Si alloy, along with the results from other Al-Si alloys examined by Hosch [3] Gunduz [17] and Magnin [33].

Figure 14 shows that the results of this analysis on Al-10wt%Si matches up well with past results of Al-Si alloys. This validates the use of the modified Jackson-Hunt approach to estimate the local eutectic growth velocity and undercooling.

A second set of the local eutectic solidification parameters, namely, the cooling rate and the thermal gradient were estimated. This estimation relied on a thermal analysis that was developed by Garcia et al. [34] and expanded on by Spinelli et al. [35], which described the 1D unidirectional solidification of metal castings. This thermal analysis involved a thermal energy balance at the solidification front, where the latent heat given off by the portion of the front that solidified had to be balanced by the conductive heat transfer at the front for solidification to progress. Using this

thermal balance, an expression was developed that described the required conditions for solidification to occur within a 1D sphere:

$$k_t \left(\frac{dT}{dr}\right)_{r=r_f} = L\rho_L \left(\frac{dr_f}{dt}\right) \quad (6)$$

Where *k* is the thermal conductivity of the liquid, *L* is the latent heat of fusion, ρ_L is the density of the liquid, *dr* is the incremental solid layer as solidification advances and r_f is the radius of the freezing solidification front [35]. For the development of this model, Garcia et al. [34] neglected the influence of convection, the changes in volume due to differing densities and superheating in the liquid.

Examining Equation 6, the $\left(\frac{dT}{dr}\right)_{r=r_f}$ term can also be expressed as the local thermal gradient (G_{eut}), while the $\left(\frac{dr_f}{dt}\right)$ term, can be expressed as the local growth velocity (v^*). Using these definitions, the thermal balance may be re-written as:

$$k_L G_{eut} = L dv^* \quad (7)$$

Based on Equation 7, a relationship between the eutectic growth velocity and the eutectic cooling rate ($CR_{eut} = G_{eut} v^*$) can be made:

$$CR_{eut} = C_1 {v^*}^2 \quad (8)$$

$$C_1 = \frac{L\rho_L}{k_L} \quad (9)$$

Where CR_{eut} is the local eutectic cooling rate and C_1, a material dependent constant.

Using Equation 8, the local eutectic cooling rate is estimated with the local growth velocity and the material constant parameter C_1, calculated using the material properties from Table 4.

Table 4: Al-Si material properties used for eutectic cooling rate estimation [36].

Parameter Symbol	Parameter Value	Unit	Parameter Name
$\boldsymbol{L}$	397300	$J.Kg$	latent heat of fusion
$\boldsymbol{\rho_L}$	2650	$Kg.m^{-1}$	density of the liquid
$\boldsymbol{k_L}$	70	$W.m^{-1}K^{-1}$	thermal conductivity of the liquid

To determine if C_1 accurately related the eutectic cooling rate to the growth velocity, Reyes et al. [37] experimentally determined the C_1 by fitting a CR_{eut} versus v^{*^2} plot [35]. From this fit it was found that the experimentally determined C_1 was $1.6\ x\ 10^7 Ksm^{-2}$, which is in good agreement with the theoretically calculated C_1 for Al-Si alloys ($1.5\ x\ 10^7 Ksm^{-2}$) [38]. This indicates that the material constant parameter, C_1 can accurately describe the relationship between the eutectic cooling rate and the eutectic growth velocity.

The estimation of the eutectic cooling rate also permitted an estimation of the local thermal gradient. This can be done by rearranging Equation 8 to make it in terms of G_{eut}:

$$G_{eut} = \frac{v^*}{CR_{eut}} \tag{10}$$

With these estimations, it is possible to map the transition in Si morphology as a function of the local eutectic solidification conditions. Thus, the Si morphology was plotted as a function of the local growth velocity and the inverse local thermal gradient. Allowing for perpendicular lines to represent the local eutectic cooling rate, which was used to define the transitions in the Si morphology. This local eutectic growth map of the Al-10wt%Si alloy can be seen in Figure 15. This mapping includes both IA and DSC results.

Figure 15 shows that Si morphology is determined by the local eutectic solidification conditions, as the refinement of the Si morphology is found to improve with increasing v^* and CR_{eut} . High v^* and CR_{eut}, results in a globular Si morphology, and as v^* and CR_{eut} decreases the Si morphology transitions from globular to fibrous to flaky. The critical cooling rates for these transitions, from flaky → fibrous, fibrous → globular + fibrous and the globular + fibrous → globular, occurred at ~60 K/s, ~350 K/s, and ~1600 K/s respectively.

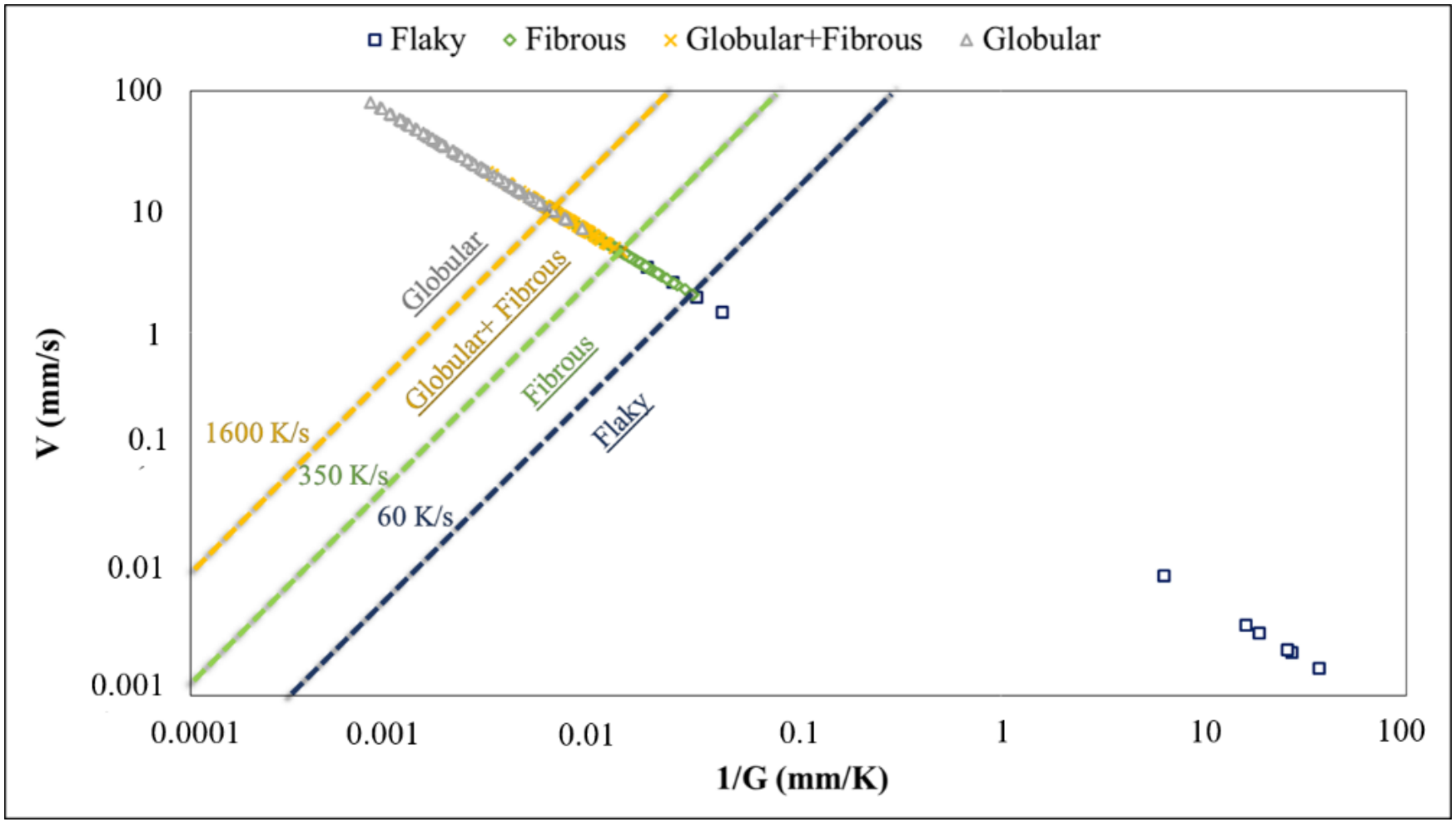

371

372 Figure 15: Local eutectic Si growth map for Al-10Si alloys.

373

374

3.4 SOLIDIFICATION CONTINUOUS COOLING TRANSFORMATION DIAGRAM (SCCT)

Figure 16 shows the SCCT diagram, mapping out the solidification pathway of the Al-10wt%Si alloy over the investigated thermal histories. The primary and eutectic nucleation temperatures and the Si morphology are shown as a function of liquid cooling rate. It can be seen that, as the undercooling increases with the cooling rate, the Si morphology varies in the following sequence.

Figure 16 provides a microstructure map that outlines the solidification path for the Al-10wt%Si alloy. This SCCT acts as a powerful tool that can identify the required solidification conditions for certain Si morphologies to form. While similar CCT & SCCT diagrams have been made for other alloy systems, such as steel, there are no such diagrams for Al alloys. As such, this SCCT provides insight into a previously un-quantified aspect, the solidification path of hypo-eutectic Al-Si alloys.

The use of the SCCT presented in Figure 16 is not restricted to solidifying liquid droplets. The use of this diagram should apply for any liquid of the Al-10wt%Si composition solidifying in any given rapid solidification process. As these rapid conditions may occur in several processes such as strip casting, die casting or additive manufacturing. Limitations to the use of this diagram will occur when there is significant segregation of Si during solidification. However, in these instances, similar SCCT diagrams may be derived using droplet cooling rates for alloys with different Si compositions, to trace the path of solidification of a given alloy in a particular process. This of course remains to be illustrated and is the subject of current research

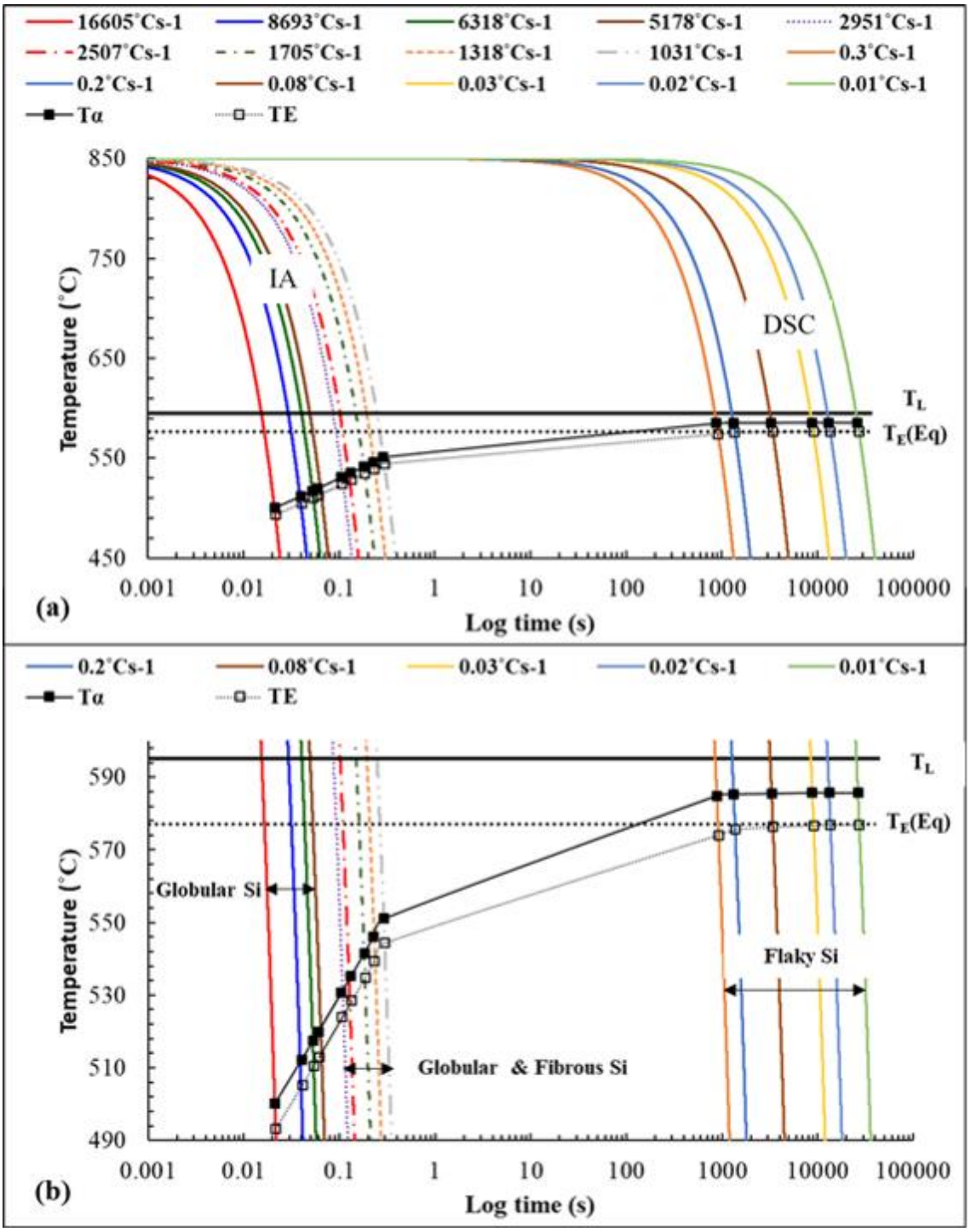

Figure 16: (a) Solidification Continuous Cooling Transformation curves of Al-10Si (b) A zoom on the variation of primary and eutectic nucleation temperature with cooling rate and the corresponding Si morphologies.

3.5 Influence of Si Morphology on Mechanical Properties

The importance of understanding the solidification path and the microstructure of an alloy is to see how they affect the mechanical properties. To examine this, Vickers hardness measurements of the Al-10wt%Si alloy were plotted as a function of the liquid cooling rate in Figure 17.

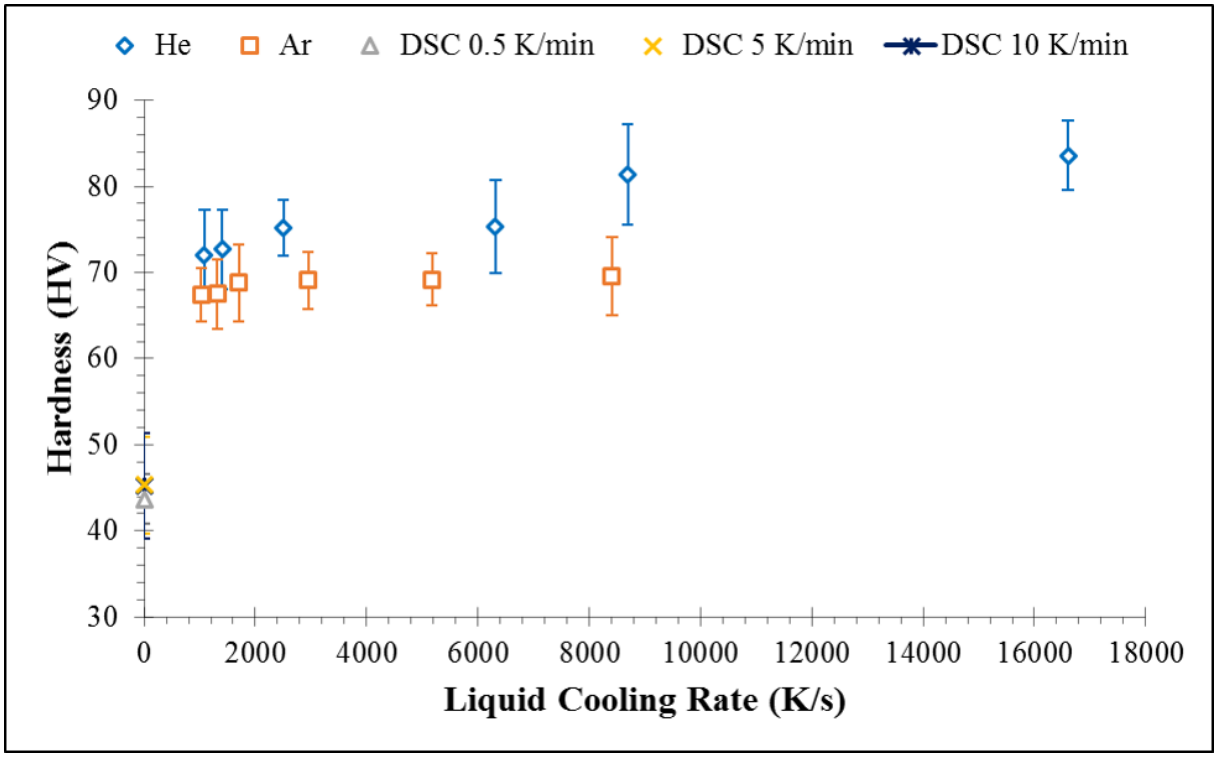

Figure 17: Vickers hardness of the Al-10Si alloy as a function of the liquid cooling rate.

The first thing Figure 17 shows is that the rapidly cooled IA samples are noticeably harder than the DSC samples. With there being a minimum improvement in the hardness of ~49% and a maximum improvement of 91%, when comparing the average hardness values.

Beyond this, there seems to be an influence of the atomization gas, as the samples atomized in helium were slightly harder than those atomized in argon. However, the influence of the liquid cooling rate was less clear, as changes in the liquid cooling rate did not lead necessarily lead to changes in the hardness. This indicated that the liquid cooling rate, alone, cannot account for variation in the Al-10wt%Si alloy hardness.

To explore this further, other aspects of the IA Al-10wt%Si alloy were related to the hardness. Starting with the interphase spacing of the pro-eutectic α-Al phase and the Si spacing of the eutectic structure. To determine if spacing refinement, of either component, influenced the Vickers

hardness a method to compare the two factors was developed using a "Hall-Petch" type relationship. Typically, a Hall-Petch relation is used to describe the strengthening of a material as the grain size decreases [39]:

$$\sigma_y = \sigma_i + \frac{k_y}{\sqrt{D_g}} \tag{11}$$

Where σ_y is the yield strength, σ_i is a materials constant for the starting stress for dislocation movement, k_y is the strengthening coefficient and D_g is the average grain diameter.

The defining characteristic of the Hall-Petch is the inverse linear relationship between the strength (σ_y) and the square root of the grain size (D_g). In this work, instead of comparing the strength of the alloy to the grain size, the hardness of the alloy was compared to the interphase spacing. For there to be a Hall-Petch relationship there needs to be a clear inverse linear trend between the hardness and the interphase spacing. If this is not present, then it could be said that the spacing did not directly contribute to the strengthening of the alloy. Using this modified "Hall-Petch" approach the spacing of the pro-eutectic α-Al phase was compared to the Al-10wt%Si alloy hardness in Figure 18.

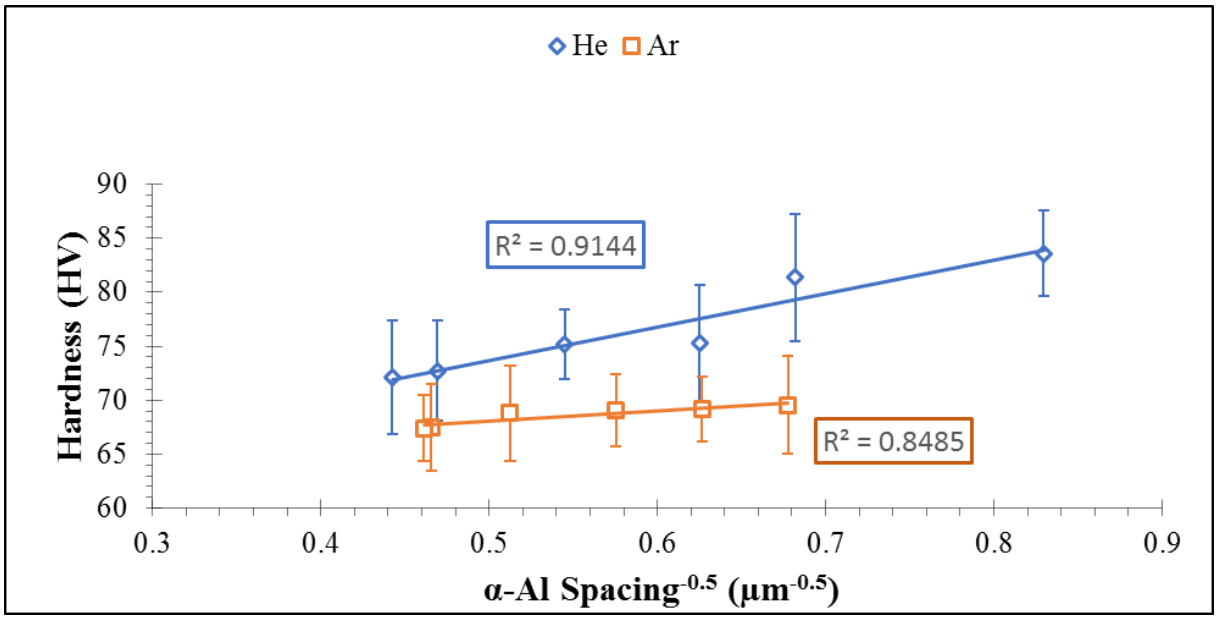

Figure 18: "Hall-Petch" hardness versus α-Al dendrite cell spacing plot for IA Al-10Si alloy.

Examining Figure 18, a Hall-Petch relationship between the hardness and the α-Al spacing is only observed when looking at the argon and helium samples separately. This means that there is not a

"Hall-Petch" relationship and that a reduction in pro-eutectic α-Al spacing, alone, cannot explain the variations in the measured hardness.

This same "Hall-Petch" approach was then used to examine the influence of the eutectic Si spacing on the alloy hardness. To conduct this comparison the eutectic Si spacing was plotted versus the hardness in a "Hall-Petch" type of plot in Figure 19.

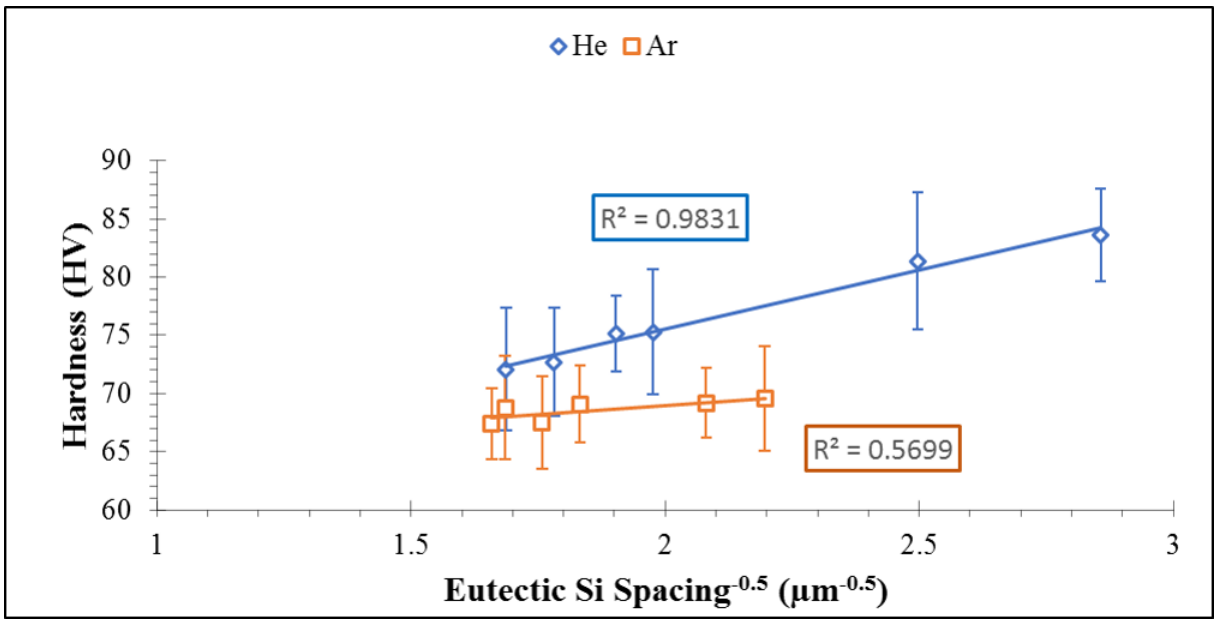

Figure 19 shows that a "Hall-Petch" relationship was observed only when looking at the argon and helium samples separately. This indicates, just as with the α-Al spacing, that there is not a "Hall-Petch" relationship between the eutectic Si spacing and the hardness. Therefore, a reduction in spacing of the eutectic Si also cannot explain the variations in the Al-10wt%Si alloy hardness.

Figure 19: "Hall-Petch" hardness versus eutectic Si spacing plot for IA Al-10Si alloy.

With these microstructural aspects proving inconclusive, this left the shifts in the Si morphology as the probable cause for the hardness variations. With that said, it was difficult to directly relate the Si morphology to the measurements of the Vickers hardness, as the indenter of the machine was too large to measure specific regions or Si morphologies. So, in order to relate the Si morphology to the alloy hardness an initial correlation, between the hardness and some other factor, had to be made first.

Previously in Figure 15 it was found that shifts in the Si morphology were related to changes in the local eutectic cooling conditions. A global aspect of solidification that is a driving force for

this local growth is the undercooling experienced prior to eutectic nucleation. So, it was thought that the eutectic nucleation undercooling could be used to relate the Si morphology to the alloy hardness. The eutectic nucleation undercooling, as well as the dominant Si morphology at each eutectic undercooling, was plotted as a function of the hardness in Figure 20.

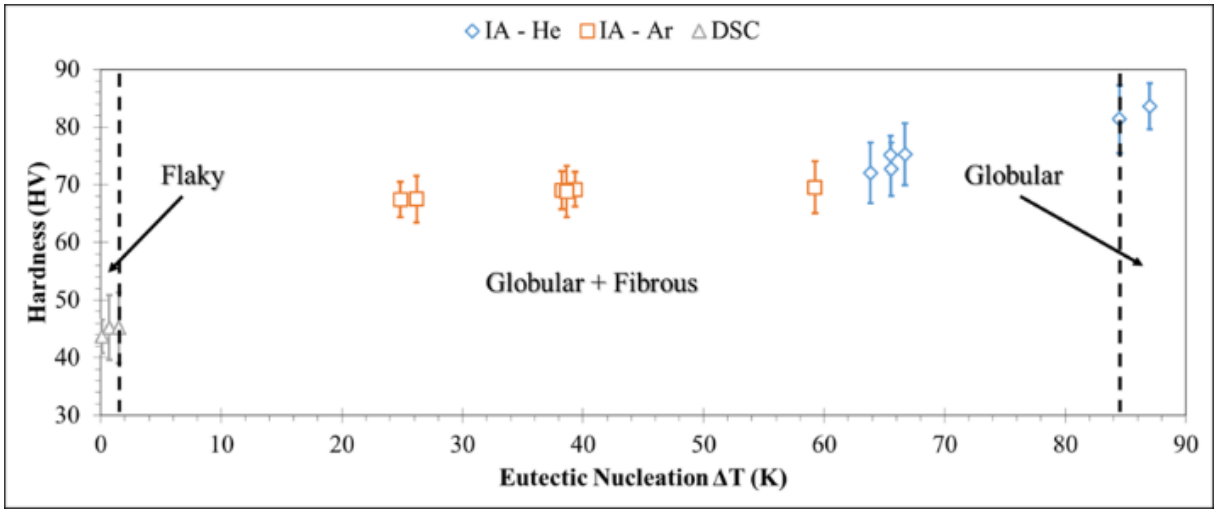

Figure 20: Influence of the eutectic nucleation undercooling and Si morphology on the Al-10Si alloy hardness.

The results in Figure 20 show that the variations in alloy hardness are a function of the Si morphology. With the highest hardness being achieved when the eutectic Si was predominantly globular. Having a globular Si morphology improved the alloy hardness by ~8.1 to 24%, when compared to a globular+fibrous morphology, and improved the alloy hardness by ~80 to 91%, when compared to a flaky morphology.

Figure 20 also highlights when shifts in the Si morphology will occur, as they are also a function of the eutectic undercooling. This correlates to results from Figure 15 which found a globular morphology would form when the growth conditions were most rapid (i.e. high undercooling).

4 CONCLUSIONS

Al-10wt%Si alloys of various thermal histories were generated by impulse atomization (IA) and Differential Scanning Calorimetry (DSC). Analysis of the micrographs confirmed the expected solidification microstructure, consisting of a pro-eutectic α-Al phase and an α-Al + Si eutectic

structure. However, the morphology of these phases (particularly the Si eutectic) was found to noticeably shift as the solidification conditions changed.

The eutectic Si phase was found to form into four distinct morphologies, labelled flaky, fibrous, globular + fibrous and globular. The globular morphology was found to be the finest while the flaky morphology was the coarsest.

This transition in the Si morphology was found to be a function of the local eutectic solidification conditions. As such, a local eutectic solidification map was constructed to relate the Si morphology to the local growth conditions. The Si morphology was found to transition from flaky → fibrous → globular + fibrous → globular at local eutectic cooling rates of ~60 K/s, ~350 K/s, and ~1600 K/s, respectively.

A solidification continuous cooling transformation (SCCT) diagram of the investigated alloy was constructed to map out the solidification path and Si morphology over a wide range of cooling rates and undercoolings, providing insight into the microstructure formation in hypo-eutectic Al-Si alloys.

It can be concluded from this work that, control of the Si morphology is very important as it affects the mechanical properties of the alloy as tremendous improvements in hardness (up to 91% in this work) is achieved when the Si morphology transitioned from flaky to globular. Even shifting the Si morphology from globular+fibrous to globular is found to improve the alloy hardness by up to ~24%. These results are a testimony that the Si morphology should be seriously considered when trying to understand the mechanical properties of hypo-eutectic Al-Si alloys.

ACKNOWLEDGMENTS

The authors wish to acknowledge funding of this work from a Collaborative Research and Development Grant from the Natural Sciences and Engineering Research Council of Canada, Equispheres Inc., and the European Space Agency (ESA)

REFERENCES

[1] Z. Li, A. Samuel, F. Samuel, C. Ravindran, S. Valtierra and H. Doty, *Materials Science and Engineering A, 2004,* vol. 367, pp. 96-110.

[2] F. Robles-Hernandez, J. Ramirez and R. Mackay, Al-Si Alloys: Automotive, Aeronautical and Aerospace Applications, Springer, 2017.

[3] T. Hosch, L. England and R. Napolitano, *Journal of Materials Science, 2009,* vol. 44, pp. 4892-4899.

[4] S. Lu and A. Hellawell, *Metallurgical Transactions A, 1987,* vol. 18, no. 10, pp. 1721-1733.

[5] A. Mazahery and M. Shabani, *JOM, 2014,* vol. 66, no. 5, pp. 726-738.

[6] N. Rathod and J. Manghani, *International Journal of Emergin Trends in Engineering and Development, 2012,* vol. 5, p. 574.

[7] S. Hegde and K. Prabhu, *Journal of Materials Science, 2008,* vol. 43, pp. 3009-3027.

[8] M. Makhlouf and H. Guthy, *Journal of Light Metals, 2001,* vol. 1, pp. 199-218.

[9] A. Hellawell, *Progress in Materials Science, 1970,* vol. 15, pp. 1-78.

[10] S. Khan and R. Elliott, *Journal of Materials Science, 1996,* vol. 31, no. 14, pp. 3731-3737.

[11] R. Trivedi, F. Jin and I. Anderson, *Acta Materialia, 2003,* vol. 51, pp. 289-300.

[12] Y. Kalay, L. Chumley, A. I and R. Napolitano, *Metallurgical and Materials Transactions A,2007,* vol. 38A, pp. 1452-1457.

[13] M. Pierantoni, M. Gremaud, P. Magnin, D. Stoll and W. Kurz, *Acta Metallurgica et Materialia, 1992,* vol. 40, no. 7, pp. 1637-1644.

[14] J. Wiskel, H. Henein and E. Maire, *Canadian Metallurgical Quarterly, 2002,* vol. 41, no. 1, pp. 97-110.

[15] A.-A. Bogno, J. Valloton, H. Henein, D. Ivey, A. Locock and M. Gallerneault, *Canadian Metallurgical Quarterly, 2018,* vol. 57, no. 2, pp. 148-159.

[16] M. Gunduz and E. Cadirli, *Materials Science & Engineering A, 2002,* vol. 327, pp. 167-185.

[17] M. Gunduz, H. Kaya, E. Cadirli and A. Ozmen, *Materials Science and Engineering , 2004,* vol. 369, pp. 215-229.

[18] K. Jackson and J. Hunt, *Trans. Am. Inst. Min. Engineers, 1966,* vol. 236, p. 1129.

[19] J. Wiskel, K. Navel, H. Henein and E. Marie, *Canadian Metallurgical Quarterly, 2002,* vol. 41, no. 2, pp. 193-204.

[20] J. Dantzig and M. Rappaz, Solidification, Boca Raton: CRC Press, 2009.

[21] C. Levi and R. Mehrabian, *Metallurgical Transactions A, 1982,* vol. 13A, pp. 13-23.

[22] A. L. Genau, Iowa State University, Ames, Iowa, 2004.

[23] H. Petersen, *Danish Atomic Energy Commision, 1970,* no. 224, pp. 6-7.

[24] C. Caceres, C. Davidson, J. Griffiths and Q. Wang, *Met. and Mat. Transactions A, 1999,* vol. 30A, pp. 2611-2618.

[25] K. Oswalt and M. Misra, *AFS Transactions, 1980,* vol. 88, pp. 845-862.

[26] P. Anyalebechi, T. Rouns and R. Sanders, *Light Metals 1991, 1991,* no. TMS 1990, pp. 821-850.

[27] A.-A. Bogno, P. D. Khatibi, H. Henein and C.-A. Gandin, *Metallurgical and Materials Transactions A, 2016,* vol. 47A, pp. 4606-4615.

[28] W. Prukkanon, N. Srisukhumbowornchai and C. Limmaneevichitr, *Jornal of Alloys and Compounds, 2009,* vol. 477, pp. 454-460.

[29] H. Jones, in *Rapid Solidification of Metals and Alloys*, London, The Institution of Metallurgists, 1983, pp. 40-43.

[30] P. Anyalebechi, *TMS, 2004,* pp. 217-233.

[31] G. Armstrong and H. Jones, Solidification and Casting of Metals, London: Metals Society, 1979.

[32] R. Grugel and W. Kurz, *Metallurgical Transactions A, 1987,* vol. 18, pp. 1137-1142.

[33] P. Magnin, J. Mason and R. Trivedi, *Acta Metallurgica et Materialia, 1991,* vol. 39, no. 4, pp. 469-480.

[34] A. Garcia, T. Clyne and M. Prates, *Metallurgical Transactions B, 1979,* vol. 10B, pp. 85-92.

[35] J. Spinelli, A.-A. Bogno and H. Henein, *Metallurgical and Materials Transactions A, 2018,* vol. 49, no. 2, pp. 550-562.

[36] Z. Zhang, X. Bian, Y. Wang and X. Liu, *Transactions of Nonferrous Metals Society of China, 2001*, vol. 11, no. 3, pp. 374-377.

[37] R. Retes, T. Bello, R. Kakitani, T. Costa, A. Garcia, N. Cheung and J. Spinelli, *Materials Science and Engineering A, 2017,* vol. 685, pp. 235-243.

[38] J. Spinelli, W. Hearn, A.-A. Bogno and H. Henein, *Light Metals 2018, 2018,* pp. 381-387.

[39] W. D. Callister Jr. and D. G. Rethwisch, Fundamentals of Materials Science and Engineering: An Integrated Approach, Hoboken: John Wiley & Sons, 2008.

List of Figure captions

Figure 1: Characteristic linear intercept measurements used to determine the eutectic Si spacing. Shown is an IA Al-10Si particle produced using helium, at a particle size of 212-250μm.

Figure 2: Characteristic linear intercept measurements used to determine the pro-eutectic α-Al spacing. Shown is an IA Al-10Si particle produced using helium, at a particle size of 212-250μm.

Figure 3: Typical microstructure of an Al-10Si alloy produced by DSC. Cooling rate: 5 K/min (~0.1 K/s). (a) Islands of primary α-Al (dark) surrounded by eutectic cells (α-Al +Si), (b) Zoom of a eutectic cell. The lightest phases are Fe-rich compounds.

Figure 4: (a) Typical microstructure of Al-10Si droplets atomized in helium (droplet size in the range 300-355 μm); (b) & (c) are higher magnification images highlighting the α-Al + Si eutectic structure.

Figure 5: *Typical microstructure of Al-10Si droplets atomized in* argon, (droplet size in the range 125-150 μm); (b) & (c) are higher magnification images highlighting the α-Al + Si eutectic structure.

Figure 6: XRD patterns for the Al-10Si alloy produced by IA.

Figure 7: Eutectic fraction of the IA Al-10Si alloy, as a function of the particle size and the atomization gas.

Figure 8: Pro-eutectic α-Al dendrite cell spacing as a function of the coarsening solidification rate. The B & n values for the IA Al-10Si alloy are shown in blue, while the ideal values for Al alloys are shown in orange. This plot also includes the B & n values for Al-Si alloys from the past work of Anyalebechi [30] and Armstrong [31].

Figure 9: Eutectic Si spacing as a function of the liquid cooling rate for the Al-10wt%Si alloy.